*Submitted to the Annals of Applied Statistics*

# INFORMATIVE AUTONOMOUS SAMPLING OF OCEANOGRAPHIC VARIABLES USING JOINT EXCURSION SETS

By Trygve Olav Fossum[1,2], Jo Eidsvik[3], David Ginsbourger[4], and Kanna Rajan[2,5,6].

[1]*Department of Marine Technology, The Norwegian University of Science and Technology (NTNU), Trondheim, Norway.*
[2]*Centre for Autonomous Marine Operations and Systems (AMOS).*
[3]*Department of Mathematical Sciences, NTNU.*
[4]*Uncertainty Quantification and Optimal Design group, Idiap Research Institute, Martigny, Switzerland.*
[5]*Department of Engineering Cybernetics, NTNU*
[6]*Underwater Systems and Technology Laboratory, Faculty of Engineering, University of Porto, Portugal.*

Improving and optimizing oceanographic sampling is a crucial task for marine science and maritime management. Faced with limited resources to understand processes in the water-column, the combination of statistics and autonomous robotics provides new opportunities for experimental designs. In this work we develop methods for efficient spatial sampling applied to the mapping of coastal processes by providing informative descriptions of spatial characteristics of ocean phenomena. Specifically, we define a design criterion based on reducing uncertainty in the joint excursions of vector-valued Gaussian random fields, and derive tractable expressions for the expected Bernoulli variance reduction in such a framework. We demonstrate how this criterion gives a description of the boundary uncertainty, that can be used to prioritize sampling efforts at locations that are ambiguous, making exploration more effective. We use simulations to study the properties of methods and to compare them with state-of-the-art approaches, followed by results from field deployments with an autonomous underwater vehicle as part of a case study mapping the boundary of a river plume. The results demonstrate the potential of combining statistical methods and robotic platforms to effectively inform and execute data-driven environmental sampling.

**1. Introduction.** Monitoring the world's oceans has gained increased importance in light of the changing climate and increasing anthropogenic impact. A central problem for understanding these factors is the lack of

*Keywords and phrases:* Ocean Sampling, Excursion Sets, Gaussian Processes, Experimental Design, Adaptive Information Gathering

representative data with sufficient resolution. Most of this *undersampling* can be attributed to the large spatio-temporal variations on which ocean processes transpire, prompting the need for effective means of sampling. By *sampling*, we refer to the design of observational strategies in the spatial domain, where the use of autonomous platforms can be combined with statistical methods to pursue measurements with high scientific relevance.

Traditional data collection at sea has typically been based on static buoys, Lagrangian floats, or ship-based methods, with significant logistical limitations that directly impact coverage and sampling resolution. Modern methods using satellite remote-sensing provide large-scale coverage but have limited resolution, are limited to sensing the surface of the ocean, and are impacted by cloud cover. The advent of robust mobile robotic platforms (Bellingham and Rajan, 2007) has resulted in significant contributions to environmental monitoring and sampling. In particular, autonomous underwater vehicles (AUVs), have advanced the state of sampling and consequently have made robotics an integral part of ocean observation; our previous work has contributed to this effort (Das et al., 2012, 2015; Fossum et al., 2019, 2018). Other statistical work in the oceanographic domain include Wikle et al. (2013) focusing on hierarchical statistical models; Sahu and Challenor (2008), studying spatio-temporal models for sea surface temperature and salinity data; and Mellucci et al. (2018) looking at the statistical prediction of features using an underwater glider.

The potential that lies in using information-based methods, which we highlight in this paper, is to do efficient environmental sampling and overcome three common challenges, namely:

- Full numerical ocean models cannot provide accurate results online if run on robotic sensing platforms, as onboard computers cannot deliver the computational power required. Hence statistical proxy models of the environment must be used for learning where to sample.
- With limited available information about the state of the ocean, there is substantial value in reacting to information obtained from measurements taken in-situ. This acquired information must be assimilated into statistical models that can be used to inform decisions on where to sample sequentially.
- For sampling problems related to environmental sensing, the number of choices (i.e. locations, trajectories, and candidate designs) is enormous, creating a trade-off between optimization (finding the most resource-efficient design to collect necessary data) and computability (arriving at a solution in reasonable time). To successfully resolve features, this trade-off has to be considered in development and practice.

Addressing this, the combination of statistical tools and robotic platforms is a natural symbiosis which enables information-based sensing. Central to this is the ability to model spatially-correlated variables and provide formal measures of uncertainty. In our formulation we use Gaussian Processes (GPs) in large part because they allow for efficient implementation and evaluation in real time onboard a robotic platform.

In this work, we build on joint excursion sets (ES) and excursion probabilities (EP) for the spatial design of experiments. The goal is to design sampling strategies for reducing the spatially-integrated Bernoulli variance (IBV) in the ES indicators. Our main contributions include: i) extending the IBV criteria to multivariate GPs, thereby allowing the evaluation to include multiple environmental parameters such as temperature and salinity; ii) developing methods for information-based environmental sensing and autonomous data collection; and iii) demonstrating the approach in the real-world scenario of sampling a river plume using an AUV.

The remainder of this paper is organized as follows: Section 2 provides select background on ocean sampling; Section 3 defines ESs, EPs, and the design criteria of IBV; Section 4 sets up the required statistical modeling assumptions of the bi-variate GPs for temperature and salinity; Section 5 builds on these assumptions when deriving the analytical derivation of the design criteria; Section 6 extends these results and present heuristics for adaptive sampling; Section 7 discusses properties of the methods in simulation studies. Section 8 demonstrates the methodology used in field work characterizing a river plume; and Section 9 contains a summary and a discussion of future work.

## 2. Background and Motivation.

2.1. *Observing Processes in the Upper Ocean.* Central to understanding the changes taking place in the upper water-column is an understanding of biophysical interaction driven by an agglomeration of physical forcing (wind, topography, bathymetry, tidal influences, and local geography, such as fresh water inflows) and incipient micro-biology driven by planktonic and coastal anthropogenic input, such as pollution and agricultural runoff transported into the ocean by rivers and streams. These often result in a range of ecosystem-related phenomena such as blooms, anoxic zones and plumes, all of which have significant direct and indirect effects on society. Walter Munk referred to the $20^{\text{th}}$ century as the *century of undersampling* (Munk, 2002), pointing out a lack of sufficient sampling resolution in time and space as a critical issue for characterizing ocean phenomena. Even today, policymakers struggle with limited observability of severe environmental problems;

a prominent example is the recent (May 2018) outbreak of harmful algal blooms in Northern Norway[1], with losses exceeding 12 million tons of salmon valued at $80 million (Norwegian Directorate of Fisheries). This is a case in point of how adequate sampling efforts could have provided a more accurate assessment and early warning of changing environmental conditions. These challenges related to undersampling have been driving ocean sensing practices towards more autonomous, networked, and distributed use of robotic assets in order to fill the gaps in our understanding (See Fig. 1(a)), where observation is guided by assimilation of recent measurements and statistical models.

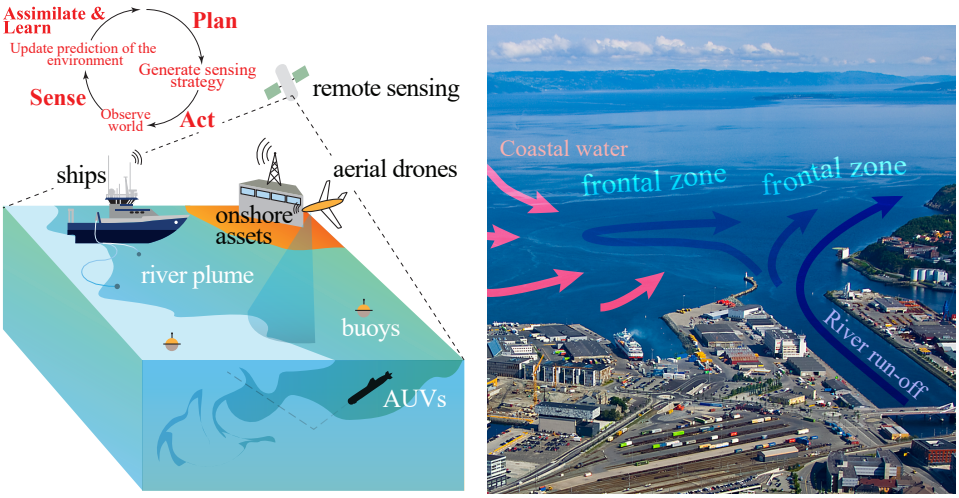


(a) Illustration of an ocean sensing network and the sense-plan-act control methodology.

(b) Frontal patterns off of the Nidelva river, Trondheim, Norway.

FIG 1. *1(a) Traditional ocean observation based on ship-based sampling has recently been augmented by autonomous and collaborative networked operations of robotic vehicles to resolve numerous bio-geochemical processes and their interactions. The sense-plan-act control approach to autonomous control can reason and make decisions for efficient onboard adaptive sampling. 1(b) The interaction of river and ocean creates processes that are challenging to map, where the combination of statistics and robotics can play a vital role in enabling more effective observation practices.*

Our focus in this work is towards spatial characterization of a frontal system specifically, fronts generated by river plumes. Fig. 1(b) shows the survey area (the outlet of the Nidelva river, Trondheim, Norway) where cold freshwater enters from the river, creating a strong gradient in both temperature and salinity. Because of the local topography and the Coreolis

[1]Report from the Institute of Marine Research: https://bit.ly/2KZGJfI

force (Coriolis, 1835) the cold fresh water tends to flow near land to the east. Depending on the river discharge, tidal effects, wind, and temperature differences, this boundary often gets distorted. Initial knowledge about the location and evolution of these features is therefore highly uncertain, making deterministic planning challenging.

River plumes belong to a class of ocean processes that are local and act on smaller *sub-mesoscale* extent (from $5m^2$ – $10km^2$) where lateral spatial variability tends to dominate. Remote sensing and synthetic ocean models often find it challenging to provide detail at this scale (Lermusiaux, 2006) and the principal way to resolve for fine resolution is by direct in-situ observation. At larger *mesoscale* ($> 50km^2$), both three-dimensional space and time dynamics are important and can shift substantially, while in the case of river plumes one can often limit the scope to cover only lateral spatial elements. However, the methodological framework can be extended to higher dimensional situations in a similar manner.

2.2. *Autonomous Vehicles.* AUVs are used to gather in-situ spatio-temporal data while carrying a range of scientific payloads to survey the water column. Typically, they operate at $\sim 1-3$ m/s, can reach depths from 100–6000 m with an in-water operation time capacity dependent on survey speed, payload sensors and mission design. By deploying AUVs together with other resources, one can augment information from synthetic ocean models, remote-sensing data, or fixed-location sensors on buoys. Traditional operations and surveys with AUVs are usually limited to observations along fixed transects on a spatial grid, pre-programmed by the human operator. A more effective approach is to instead use onboard algorithms to continuously evaluate, update, and refine future sampling locations (sense-plan-act cycle in Fig. 1(a)), making the information gathering *adaptive* and *contextual* to the survey requirements (Das et al., 2012; Fossum et al., 2019, 2018). The space of sampling opportunities can still be limited to a grid, but adaptation allows more flexibility. For instance, an AUV could reconstruct or modify a survey line based on what temperatures it is measuring by using embedded methods in decision-theoretic planning (Py, Rajan and McGann, 2010; Rajan and Py, 2012; Rajan, Py and Berreiro, 2012).

Adaptive sampling of an evolving frontal feature has been explored in Gottlieb et al. (2012); Zhang et al. (2012); Pinto et al. (2018); Costa et al. (2018). These approaches typically use a reactive-adaptive scheme, whereby exploration does not rely on a statistical model of the environment, but rather adapts based on closing the sensing and actuation loop. Myopic sampling, i.e. stage-wise selection of the path (on the graph) which reduces the

information criterion the most, has been used for adaptive surveys (Singh et al., 2009; Binney, Krause and Sukhatme, 2013) that focus largely on reducing predictive variance or mutual information (e.g. entropy). Variance and entropy reduction are independent of the actual data realizations under the assumptions of GP models; the use of data-driven adaptive criteria was introduced to include more targeted sampling of regions of scientific interest in Low, Dolan and Khosla (2009) and Fossum et al. (2018). In this paper, with a focus on mapping the river plume, we reward the designs that improve the classification of water masses as a means to characterize the frontal zone and thereby the extent of the river plume.

**3. Excursion Sets and Integrated Bernoulli Variance.** Our objective is to leverage statistical tools to characterize a river plume, focusing on spatial separation of cold freshwater from the river and warmer saline waters of the fjord. ES and EPs are useful starting points to measure the ability to classify water masses. The goal of experimental sampling is to improve this characterization, as quantified via changes in the EPs.

We consider a lateral domain near the sea surface, with locations $\boldsymbol{x} \in \mathcal{M} \subset \mathbf{R^2}$. The two variables of interest, temperature and salinity, are defined as random processes: $\xi_T(\boldsymbol{x})$ denotes the temperature (in $^oC$) and $\xi_S(\boldsymbol{x})$ denotes the salinity (in $g/kg$) at location $\boldsymbol{x}$. The generalization to more than two variables is given in Section 5.3, and the adaptive sampling strategies are described in Section 6.

We let $t_T$ be a threshold for temperature and $t_S$ a threshold for salinity. The joint ES is then defined by:

$$\text{ES} = \{\boldsymbol{x} \in \mathcal{M} | \xi_T(\boldsymbol{x}) \leq t_T, \xi_S(\boldsymbol{x}) \leq t_S\}. \tag{1}$$

The excursions could also be defined as larger than a threshold, or within a boundary of limits for the two variables; calculations and interpretations will be similar in these cases.

The ES holds random indicator variables while the associated EPs are:

$$p(\boldsymbol{x}) = P(\xi_T(\boldsymbol{x}) \leq t_T, \xi_S(\boldsymbol{x}) \leq t_S), \quad \boldsymbol{x} \in \mathcal{M}. \tag{2}$$

If the EPs in Eq. (2) are close to 1 or 0 at a given location, it is easy to classify water mass at this point as either river or ocean; it is, however, challenging if the probability is close to 0.5. The IBV, see Bect, Bachoc and Ginsbourger (2019), is defined as:

$$V = \int_{\boldsymbol{x} \in \mathcal{M}} p(\boldsymbol{x}) \left(1 - p(\boldsymbol{x})\right) d\boldsymbol{x}. \tag{3}$$

Data can be gathered at selected locations of the domain $\mathcal{M}$, to improve classification performance. We denote temperature measurements by $y_T(\boldsymbol{x}_i)$ and salinity measurements by $y_S(\boldsymbol{x}_i)$ at a sampling location $\boldsymbol{x}_i \in \mathcal{M}$. Given a set of measurements denoted $\boldsymbol{y}$, the conditional EPs are:

$$p(\boldsymbol{x}; \boldsymbol{y}) = P(\xi_T(\boldsymbol{x}) \leq t_T, \xi_S(\boldsymbol{x}) \leq t_S | \boldsymbol{y}). \tag{4}$$

Our goal is to construct adaptive sampling strategies based on continuous evaluation of the EPs. As the EPs provide a description of the boundary uncertainty, the strategies can effectively use this description to prioritize sampling efforts at locations that are ambiguous, making exploration more effective. It is natural to evaluate the expected reduction in the IBV, conditioned on the survey data. The expected updated IBV is:

$$V_{\text{upd}} = \int_{\boldsymbol{x} \in \mathcal{M}} E_{\boldsymbol{y}} \left( p(\boldsymbol{x}; \boldsymbol{y}) \left( 1 - p(\boldsymbol{x}; \boldsymbol{y}) \right) \right) d\boldsymbol{x}, \tag{5}$$

where the expectation is over the planned data, and the probability is defined in Eq. (4). Considering a set $\mathcal{J}$ of possible designs for an AUV survey, a criterion for the selection is:

$$j^* = \text{argmin}_{j \in \mathcal{J}} V_{\text{upd}}(j), \tag{6}$$

where the criterion $V_{\text{upd}}(j)$ in Eq. (5) is computed for each of the possible designs.

Recent work on ESs and EPs connected to spatial statistics include Picheny et al. (2010); French et al. (2013); Bolin and Lindgren (2015); French and Hoeting (2016). Our focus is on ES as defined in Eq. (1) and the uncertainty reduction achieved by sampling as in Eq. (5). In this sense, our work is similar to Bect et al. (2012), Chevalier et al. (2014), and Azzimonti et al. (2016) who describe analytical results for the IBV for univariate processes. A major contribution of our work is to derive closed-form results for this design criteria for situations where the underlying model is based on multivariate GPs.

**4. Gaussian Processes and Excursion Probabilities.** Calculations of the EPs and the IBV require a model specification. We use GP models, which provide a practical and popular probabilistic approach to modeling environmental data, and allows a closed form evaluation of the IBVs as derived in Section 5. GPs can also be fitted to run onboard robotic vehicles with limited computational assets, such as AUVs.

4.1. *Bivariate GPs.* The Gaussian model is used to represent the bivariate random fields of temperature and salinity. At location $\boldsymbol{x} \in \mathcal{M}$, the bivariate distribution is:

$$\begin{bmatrix}\xi_T(\boldsymbol{x})\\ \xi_S(\boldsymbol{x})\end{bmatrix} \sim N\left(\begin{bmatrix}\mu_T(\boldsymbol{x})\\ \mu_S(\boldsymbol{x})\end{bmatrix}, \begin{bmatrix}\sigma_T^2(\boldsymbol{x}) & \sigma_T(\boldsymbol{x})\sigma_S(\boldsymbol{x})\gamma(\boldsymbol{x})\\ \sigma_T(\boldsymbol{x})\sigma_S(\boldsymbol{x})\gamma(\boldsymbol{x}) & \sigma_S^2(\boldsymbol{x})\end{bmatrix}\right), \tag{7}$$

where the notation refers to Gaussian (i.e. normal) distributed variables specified by the mean vector and covariance matrix. For the application of a river plume, the model parameters are specified from a short preliminary survey. The means vary with location, capturing the variability near the river mouth, while the variance parameters and correlation between salinity and temperature are assumed to be constant for all locations.

For the spatial dependence among variables, we assume a separable correlation function with the same decay for salinity and temperature, which is consistent with expectations for a river plume where the decay is related to common water masses (Section 8). In the resulting function, we have:

$$\mathrm{Cov}(\xi_i(\boldsymbol{x}), \xi_j(\boldsymbol{x}')) = \rho(\boldsymbol{x}, \boldsymbol{x}')\sigma_i\sigma_j(\gamma + (1-\gamma)\delta_{ij}), \tag{8}$$

where for $i, j \in T, S$ and $\delta_{ij} = 1$ if $i = j$, and $\delta_{ij} = 0$ otherwise. Moreover, we assume stationary isotropic random fields where the correlation function $\rho(\boldsymbol{x}, \boldsymbol{x}')$ solely depends on $\boldsymbol{x}$ and $\boldsymbol{x}'$ via Euclidean distance $h = \sqrt{||\boldsymbol{x} - \boldsymbol{x}'||^2}$. With data and prior knowledge, one could possibly fit and estimate parameters of non-stationary or non-isotropic covariance functions and more complex multivariate spatial covariance functions (Gneiting, Kleiber and Schlather, 2010; Genton et al., 2015); however, that is left for future work.

We discretize the spatial domain $\mathcal{M}$ to a set of $n$ grid locations $\mathcal{M}_g = \{\boldsymbol{x}_i, i = 1, \ldots, n\}$, where each cell has area $\Delta$; the grid is used for the waypoint graph setting the possible design locations. It is also used when solving integral expressions in Eq. (3) and (5), which are then approximated by sums over all grid cells. Using vector notation, we denote the Gaussian temperature and salinity variables on the grid and its density function by the formula:

$$\boldsymbol{\xi} = (\xi_T(\boldsymbol{x}_1), \xi_S(\boldsymbol{x}_1), \ldots, \xi_T(\boldsymbol{x}_n), \xi_S(\boldsymbol{x}_n))^t, \quad \boldsymbol{\xi} \sim N(\boldsymbol{\mu}, \boldsymbol{\Sigma}). \tag{9}$$

The length $2n$ vector $\boldsymbol{\mu}$ contains the expected values of temperature and salinity at the grid locations, while the $2n \times 2n$ matrix $\boldsymbol{\Sigma}$ contains the variance-covariances of temperature and salinity variables at all grid locations.

4.2. *Data Model and Updating of GPs.* Data are gathered by an AUV that can measure temperature and salinity at a subset of locations on the defined grid. This can be done in a static manner (where the survey design is pre-planned), or in a sequential way with several stages of data gathering. For the latter, a stage of data is gathered first, and then assimilated to get an updated model. Then the updated model is used to design and select the next stage of measurements, and so on (Section 6). Below, we describe the model for one stage of data and the Gaussian formula for a single update.

We denote the data at $n_y$ locations by $\boldsymbol{y} = (y_{T,1}, y_{S,1}, \ldots, y_{T,n_y}, y_{S,n_y})^t$, representing the temperature and salinity measurements gathered at the first stage of nodes in the grid. The conditional model for the data, given the true temperature and salinity, is described by:

$$\boldsymbol{y}|\boldsymbol{\xi} \sim N(\boldsymbol{G}\boldsymbol{\xi}, \boldsymbol{R}), \tag{10}$$

where $\boldsymbol{G}$ is a $2n_y \times 2n$ matrix containing '1's on the measurement indices of the grid and '0' otherwise. The size $2n_y \times 2n_y$ covariance matrix $\boldsymbol{R}$ contains diagonal entries $r_T^2$ and $r_S^2$ which are measurement error variances of temperature and salinity observations.

The GP mean and covariance in Eq. (9) are updated in the model when more information is available. The updated distribution for temperature and salinity variables on the spatial grid, given survey data $\boldsymbol{y}$, is Gaussian with mean and covariance:

$$\begin{aligned} \boldsymbol{m} &= \boldsymbol{m}(\boldsymbol{y}) = \boldsymbol{\mu} + \boldsymbol{\Sigma}\boldsymbol{G}^t(\boldsymbol{G}\Sigma\boldsymbol{G}^t + \boldsymbol{R})^{-1}(\boldsymbol{y} - \boldsymbol{G}\boldsymbol{\mu}), \\ \boldsymbol{A} &= \boldsymbol{\Sigma} - \boldsymbol{\Sigma}\boldsymbol{G}^t(\boldsymbol{G}\boldsymbol{\Sigma}\boldsymbol{G}^t + \boldsymbol{R})^{-1}\boldsymbol{G}\boldsymbol{\Sigma}. \end{aligned} \tag{11}$$

The updated bivariate distribution at a grid location $\boldsymbol{x} \in \mathcal{M}_g$ is then:

$$\begin{bmatrix} \xi_T(\boldsymbol{x}) \\ \xi_S(\boldsymbol{x}) \end{bmatrix} |\boldsymbol{y} \sim N\left( \begin{bmatrix} m_T(\boldsymbol{x}) \\ m_S(\boldsymbol{x}) \end{bmatrix}, \begin{bmatrix} a_T^2(\boldsymbol{x}) & a_{T,S}(\boldsymbol{x}) \\ a_{T,S}(\boldsymbol{x}) & a_S^2(\boldsymbol{x}) \end{bmatrix} \right), \tag{12}$$

with entries extracted from the conditional mean and covariance expressions in Eq. (11).

The calculation of the design criterion in Eq. (5) requires the marginal distribution of the data which is defined over $\boldsymbol{\xi}$ to be $\boldsymbol{y} \sim N(\boldsymbol{G}\boldsymbol{\mu}, \boldsymbol{G}\boldsymbol{\Sigma}\boldsymbol{G}^t + \boldsymbol{R})$. However, it turns out that a simplified form of the calculation is possible because the conditional mean in Eq. (12) is a linear (affine) function of the data $\boldsymbol{y}$ and the covariance is not a function of the data. Before inputting the data, the distribution of the conditional mean is:

$$\boldsymbol{m} \sim N(\boldsymbol{\mu}, \boldsymbol{\Psi}), \quad \boldsymbol{\Psi} = \boldsymbol{\Sigma}\boldsymbol{G}^t(\boldsymbol{G}\boldsymbol{\Sigma}\boldsymbol{G}^t + \boldsymbol{R})^{-1}\boldsymbol{G}\boldsymbol{\Sigma}. \tag{13}$$

When considering only grid location $\boldsymbol{x}$, we can extract elements from its mean vector and covariance matrix to get the bivariate distribution:

$$\boldsymbol{m}(\boldsymbol{x}) \sim N\left(\begin{bmatrix}\mu_T(\boldsymbol{x})\\ \mu_S(\boldsymbol{x})\end{bmatrix}, \begin{bmatrix}\psi_T^2(\boldsymbol{x}) & \psi_{T,S}(\boldsymbol{x})\\ \psi_{T,S}(\boldsymbol{x}) & \psi_S^2(\boldsymbol{x})\end{bmatrix}\right), \tag{14}$$

which is important for the derivation of the closed-form solution of the design criteria.

## 5. Uncertainty reduction in excursion sets.

5.1. *EPs for GPs.* Based on Gaussian modeling assumptions, the EPs can be computed at any location $\boldsymbol{x}$. Without additional data, Eq. (2) gives:

$$\begin{aligned} p(\boldsymbol{x}) &= P(\xi_T(\boldsymbol{x}) \le t_T, \xi_S(\boldsymbol{x}) \le t_S) \\ &= \Phi_2\left(\begin{bmatrix}t_T\\ t_S\end{bmatrix}; \begin{bmatrix}\mu_T(\boldsymbol{x})\\ \mu_S(\boldsymbol{x})\end{bmatrix}, \begin{bmatrix}\sigma_T^2(\boldsymbol{x}) & \sigma_T(\boldsymbol{x})\sigma_S(\boldsymbol{x})\gamma(\boldsymbol{x})\\ \sigma_T(\boldsymbol{x})\sigma_S(\boldsymbol{x})\gamma(\boldsymbol{x}) & \sigma_S^2(\boldsymbol{x})\end{bmatrix}\right), \end{aligned} \tag{15}$$

where $\Phi_2$ is the bivariate Gaussian cumulative distribution function, and the mean and covariance entries are as defined in Eq. (7).

When data $\boldsymbol{y}$ are available, Eq. (4) similarly gives:

$$\begin{aligned} p(\boldsymbol{x};\boldsymbol{y}) &= P(\xi_T(\boldsymbol{x}) \le t_T, \xi_S(\boldsymbol{x}) \le t_S|\boldsymbol{y}) \\ &= \Phi_2\left(\begin{bmatrix}t_T\\ t_S\end{bmatrix}; \begin{bmatrix}m_T(\boldsymbol{x})\\ m_S(\boldsymbol{x})\end{bmatrix}, \begin{bmatrix}a_T^2(\boldsymbol{x}) & a_{T,S}(\boldsymbol{x})\\ a_{T,S}(\boldsymbol{x}) & a_S^2(\boldsymbol{x})\end{bmatrix}\right), \end{aligned} \tag{16}$$

with parameters as defined in Eq. (11) and (12). Here, the probabilities would not only depend on the data but also on the data design defined via matrix $\boldsymbol{G}$ in Eq. (10). We next derive results that simplify the comparison of several designs.

5.2. *Expected IBV for Bivariate Models.* We will next derive closed-form solutions for the expectation in Eq. (5). The location index $\boldsymbol{x}$ is suppressed to avoid overly complex notation. We present new results for computing the expectation in the integral of Eq. (5).

A critical first element in the derivation is using the GP model and the linear dependence on $\boldsymbol{y}$ in the conditional mean in Eq. (11). This results in a closed form Gaussian distribution for the conditional mean in Eq. (14). The high-dimensional inner integral in Eq. (5) then reduces to a bivariate integral (Bhattacharjya, Eidsvik and Mukerji, 2013; Chevalier et al., 2014), with an expectation over $\boldsymbol{m} = (m_T, m_S)^t$. We standardize the two variables in Eq.

(5) as $Z_T = \frac{\xi_T - m_T}{a_T}$, $Z_S = \frac{\xi_S - m_S}{a_S}$, with $\text{Corr}(Z_T, Z_S) = a_{T,S}/(a_T a_S) = \eta_{T,S}$, and we can then rephrase the probability as:

$$\begin{aligned} P(\xi_T \le t_T, \xi_S \le t_S | \boldsymbol{y}) &= P\left(Z_T \le \frac{t_T - m_T}{a_T}, Z_S \le \frac{t_S - m_S}{a_S} | \boldsymbol{y}\right) \\ &= \Phi_2\left(\begin{bmatrix} \frac{t_T - m_T}{a_T} \\ \frac{t_S - m_S}{a_S} \end{bmatrix}; \begin{bmatrix} 0 \\ 0 \end{bmatrix}, \begin{bmatrix} 1 & \eta_{s,t} \\ \eta_{s,t} & 1 \end{bmatrix}\right) \\ &= P(\xi_T \le t_T, \xi_S \le t_S | \boldsymbol{m}). \end{aligned} \tag{17}$$

Since the expression only depends on $\boldsymbol{y}$ via its affine function $\boldsymbol{m}$, the expectation in Eq. (5) is reduced to a bivariate integral over $\boldsymbol{m}$. Introducing $\pi(\boldsymbol{m})$ for the density function of $\boldsymbol{m}$, the expected Bernoulli variance becomes:

$$\begin{aligned} E_{\boldsymbol{y}}(p(1-p)) &= E_{\boldsymbol{m}}(p(1-p)), \quad p = P(\xi_T \le t_T, \xi_S \le t_S | \boldsymbol{m}) \\ E_{\boldsymbol{m}}(p(1-p)) &= \int p(1-p)\pi(\boldsymbol{m})d\boldsymbol{m}, \\ &= \int P(\xi_T \le t_T, \xi_S \le t_S | \boldsymbol{m})\pi(\boldsymbol{m})d\boldsymbol{m} \\ &- \int P(\xi_T \le t_T, \xi_S \le t_S | \boldsymbol{m}) P(\xi_T \le t_T, \xi_S \le t_S | \boldsymbol{m})\pi(\boldsymbol{m})d\boldsymbol{m}. \end{aligned} \tag{18}$$

We will next extend results of Chevalier et al. (2014) to solve for these two parts (see also Stroh (2018)).

For the first part of the integral above, we have:

$$\int P(\xi_T \le t_T, \xi_S \le t_S | \boldsymbol{m})\pi(\boldsymbol{m})d\boldsymbol{m} = P\left(Z_T \le \frac{t_T - m_T}{a_T}, Z_S \le \frac{t_S - m_S}{a_S}\right).$$

The standardized variable $\boldsymbol{Z} = (Z_T, Z_S)$ is chosen to be independent of $\boldsymbol{m}$. Using Eq. (14), we have:

$$E(a_T Z_T + m_T - t_T) = \mu_T - t_T, \quad \text{Var}(a_T Z_T + m_T - t_T) = a_T^2 + \psi_T^2 \tag{19}$$

for the temperature part; the same holds for salinity. From this we get:

$$\begin{aligned} P &\left(Z_T \le \frac{t_T - m_T}{a_T}, Z_S \le \frac{t_S - m_S}{a_S}\right) \\ &= \Phi_2\left(\begin{bmatrix} 0 \\ 0 \end{bmatrix}; \begin{bmatrix} \mu_T - t_T \\ \mu_S - t_S \end{bmatrix}, \begin{bmatrix} a_T^2 + \psi_T^2 & a_{T,S} + \psi_{T,S} \\ a_{T,S} + \psi_{T,S} & a_T^2 + \psi_T^2 \end{bmatrix}\right). \end{aligned} \tag{20}$$

For the second part of the expression Eq.(18), standardization implies that:

$$\int P(\xi_T \le t_T, \xi_S \le t_S | \boldsymbol{m}) P(\xi_T \le t_T, \xi_S \le t_S | \boldsymbol{m}) p(\boldsymbol{m}) d\boldsymbol{m} = \tag{21}$$

$$P\left(Z_{1,T} \le \frac{t_T - m_T}{a_T}, Z_{1,S} \le \frac{t_S - m_S}{a_S}, Z_{2,S} \le \frac{t_T - m_T}{a_T}, Z_{2,S} \le \frac{t_S - m_S}{a_S}\right).$$

Here, $\boldsymbol{Z}_1 = (Z_{1,T}, Z_{1,S})$, $\boldsymbol{Z}_2 = (Z_{2,T}, Z_{2,S})$ are independent bivariate zero-mean and unit-variance Gaussian vectors, both with element-wise correlation $\eta_{T,S}$. Moreover, $\boldsymbol{Z}_1$ and $\boldsymbol{Z}_2$ are chosen to be independent of $\boldsymbol{m}$, hence:

$$\begin{pmatrix} Z_{1,T} \\ Z_{1,S} \\ Z_{2,T} \\ Z_{2,S} \\ m_T \\ m_S \end{pmatrix} \sim N\left( \begin{pmatrix} 0 \\ 0 \\ 0 \\ 0 \\ \mu_T \\ \mu_S \end{pmatrix}, \begin{bmatrix} 1 & \eta_{T,S} & 0 & 0 & 0 & 0 \\ \eta_{T,S} & 1 & 0 & 0 & 0 & 0 \\ 0 & 0 & 1 & \eta_{T,S} & 0 & 0 \\ 0 & 0 & \eta_{T,S} & 1 & 0 & 0 \\ 0 & 0 & 0 & 0 & \psi_T^2 & \psi_{T,S} \\ 0 & 0 & 0 & 0 & \psi_{T,S} & \psi_S^2 \end{bmatrix} \right). \tag{22}$$

The solution to the second part of Eq. (22) can be found by evaluating a four-variable cumulative distribution function associated with Eq. (21), accounting for the mean, variance and covariances of $\boldsymbol{Z}_1$, $\boldsymbol{Z}_2$ and $\boldsymbol{m}$ in the appropriate linear combinations. Using vector-matrix formulations, we define the linear combinations:

$$\boldsymbol{V} = \begin{bmatrix} a_T & 0 & 0 & 0 & 1 & 0 \\ 0 & a_S & 0 & 0 & 0 & 1 \\ 0 & 0 & a_T & 0 & 1 & 0 \\ 0 & 0 & 0 & a_S & 0 & 1 \end{bmatrix} \begin{pmatrix} Z_{1,T} \\ Z_{1,S} \\ Z_{2,T} \\ Z_{2,S} \\ m_T \\ m_S \end{pmatrix}, \tag{23}$$

which in turn then becomes:

$$\begin{aligned} & P\left( Z_{1,T} \leq \frac{t_T - m_T}{a_T}, Z_{1,S} \leq \frac{t_S - m_S}{a_S}, Z_{2,S} \leq \frac{t_T - m_T}{a_T}, Z_{2,S} \leq \frac{t_S - m_S}{a_S} \right) \\ = \; & \Phi_4\left( \begin{bmatrix} t_T \\ t_S \\ t_T \\ t_S \end{bmatrix}; E(\boldsymbol{V}), Var(\boldsymbol{V}) \right). \end{aligned} \tag{24}$$

The multivariate cumulative probabilities in two and four dimensions are computationally efficient using methods developed by Genz and Bretz (2009). In the end, the first part in Eq. (20) and the second in Eq. (21) are computed for each location on the grid and summed over $\boldsymbol{x} \in \mathcal{M}_g$, to get the design evaluation criterion in Eq. (5).

5.3. *Generalization to the Multivariate Case.* In our application domain with the variables temperature and salinity, the solutions to the complex integral equations for the expected IBV are reduced to calculating bi-variate and four-variate cumulative distribution functions for Gaussian vectors. For

the more general case, one would be interested in $K$ random fields. In the ocean sciences, the variables could include chlorophyll or other biogeochemical quantities in addition to temperature and salinity.

The equations derived in the previous section can then be generalized. Let $\boldsymbol{\xi}(\boldsymbol{x}) = (\xi_1(\boldsymbol{x}), \ldots, \xi_K(\boldsymbol{x}))$, and the expected Bernoulli variance is:

$$E_{\boldsymbol{y}}(p(\boldsymbol{x};\boldsymbol{y})(1-p(\boldsymbol{x};\boldsymbol{y}))), \quad p(\boldsymbol{x};\boldsymbol{y}) = P(\xi_k(\boldsymbol{x}) \leq t_k; k = 1, \ldots, K|\boldsymbol{y}). \tag{25}$$

From the first key result of linear combination of Gaussian variables, we reduce the integral to a $K$ dimensional integral of the relevant $\boldsymbol{m} = E(\boldsymbol{\xi}(\boldsymbol{x})|\boldsymbol{y})$. Next, reducing the integral to two parts, we standardize the variables and compute cumulative distributions. In summary, we get:

$$E_{\boldsymbol{y}}(p(\boldsymbol{x})(1-p(\boldsymbol{x}))) = \Phi_K\left(\begin{bmatrix} t_1 \\ \vdots \\ t_K \end{bmatrix}; \boldsymbol{\mu}, \boldsymbol{A}+\boldsymbol{\Psi}\right) - \Phi_{2K}\left(\begin{bmatrix} t_1 \\ \vdots \\ t_K \\ t_1 \\ \vdots \\ t_K \end{bmatrix}; E(\boldsymbol{V}), Var(\boldsymbol{V})\right),$$

where $\boldsymbol{A}$ and $\boldsymbol{\Psi}$ are direct $K$-variate extensions of the matrices in Eq. (20), and the matrix $\boldsymbol{V}$ finds the relevant linear combination of two independent vectors $\boldsymbol{Z}_l = (Z_{l,1}, \ldots, Z_{l,K})$, $l = 1, 2$ and $\boldsymbol{m}$, as an extension of Eq. (23).

5.4. *An Example of IBV using Temperature and Salinity.* In this section, we calculate EPs and the Bernoulli variance for a few bivariate Gaussian distributions to illustrate the concepts articulated above. Fig. 2 shows contour plots of three different densities with increasing correlation $\gamma$ between temperature and salinity. Here, the thresholds are set equal to the mean $\mu_T = t_T = 5^oC$, and salinity $\mu_S = t_S = 30$ mg/l. The displayed densities have unit standard deviations for both temperature and salinity, but we also study the effect of doubling the standard deviations.

Table 1 shows the initial EPs and the associated Bernoulli variance (second row) for the examples indicated in Fig. 2. The EPs increase with the correlation as there is a strong tendency to have concurrently low temperature and salinity. The Bernoulli variance is similarly large for high correlations. EPs and Bernoulli variances are the same for standard deviation 1 or 2, which implies that high variability in temperature and salinity is not captured in the $p(1-p)$ expression.

Table 1 (bottom two rows) shows results of expected Bernoulli variance calculations. This is presented for a design gathering both data types

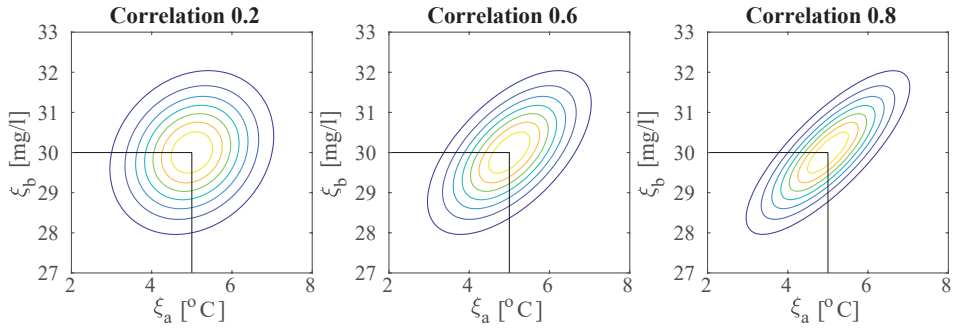


FIG 2. *Density contour plots with different correlations between temperature and salinity. The densities have unit variance and the thresholds are identical to the mean values* $5^oC$ *and* $30mg/l$*. X-axis is temperature and y-axis is salinity.*

TABLE 1. *EP and Bernoulli variance for different correlations and variances (top rows), and expected Bernoulli variances for both temperature and salinity data* $\boldsymbol{y}$ *and temperature* $y_T$ *(bottom rows).*

| | $\sigma_S = \sigma_T = 1$ | | | $\sigma_S = \sigma_T = 2$ | | |
|---|---|---|---|---|---|---|
| Correlation $\gamma$ | 0.2 | 0.6 | 0.8 | 0.2 | 0.6 | 0.8 |
| $p$ | 0.28 | 0.35 | 0.40 | 0.28 | 0.35 | 0.40 |
| $p(1-p)$ | 0.20 | 0.23 | 0.24 | 0.20 | 0.23 | 0.24 |
| $E_{\boldsymbol{y}}(p(\boldsymbol{y})(1-p(\boldsymbol{y})))$ | 0.092 | 0.089 | 0.085 | 0.052 | 0.051 | 0.049 |
| $E_{y_T}(p(y_T)(1-p(y_T)))$ | 0.151 | 0.138 | 0.123 | 0.137 | 0.114 | 0.093 |

$(y_T, y_S)$, and for a design with temperature measurements $y_T$ alone. With both data, $(y_T, y_S)^t = (\xi_T, \xi_S)^t + N(0, 0.5^2\boldsymbol{I})$, while $y_T = \xi_T + N(0, 0.5^2)$ when only temperature is measured. For this illustration, Table 1 shows that the expected Bernoulli variance gets lower with larger standard deviations $\sigma_T$ and $\sigma_S$ (right columns). The reduction of Bernoulli variance is largest for the cases with high correlation $\gamma$. Albeit smaller, there is also uncertainty reduction when only temperature is measured (bottom row), especially when temperature and salinity are highly correlated. When correlation is low ($\gamma = 0.2$), there is little information about salinity in the temperature data, and therefore less uncertainty reduction. In an application with fresh cold water from a river source, the temperature and salinity variables will not only be interdependent, but will also likely show dependence in the spatial dimension. This in turn will impact the design criteria when we evaluate the information measure by integrating over several locations (Section 8).

**6. Sequential updating and heuristic path planning.** An important concept underlying this work is the potential of robotic sampling to

adapt survey plans based on data and statistical methods in accordance with the sense-plan-act control loop (Fig. 1(a)). We will therefore present a few adaptive strategies for robotic sampling that build on the notion of multivariate ES.

6.1. *Optimal Sequential Design.* An adaptive AUV survey is split into many stages. The selection –on where to sample– is made on the graph and defined by the nearest grid nodes in the domain $\mathcal{M}_g$.

The optimal sequential design not only considers the best current AUV grid node, but also how the data gathered at this node could inform future sampling at successive stages. Let $d^{j,s}$ denote design number $j$ at stage $s$ of a sequential survey. If this design is selected, data $\boldsymbol{y}^{j,s}$ will be gathered. The optimal path selection situation is depicted in Fig. 3, where design choices are indicated by squares while data realizations are indicated by circles. The mathematical expression for the optimal design then involves

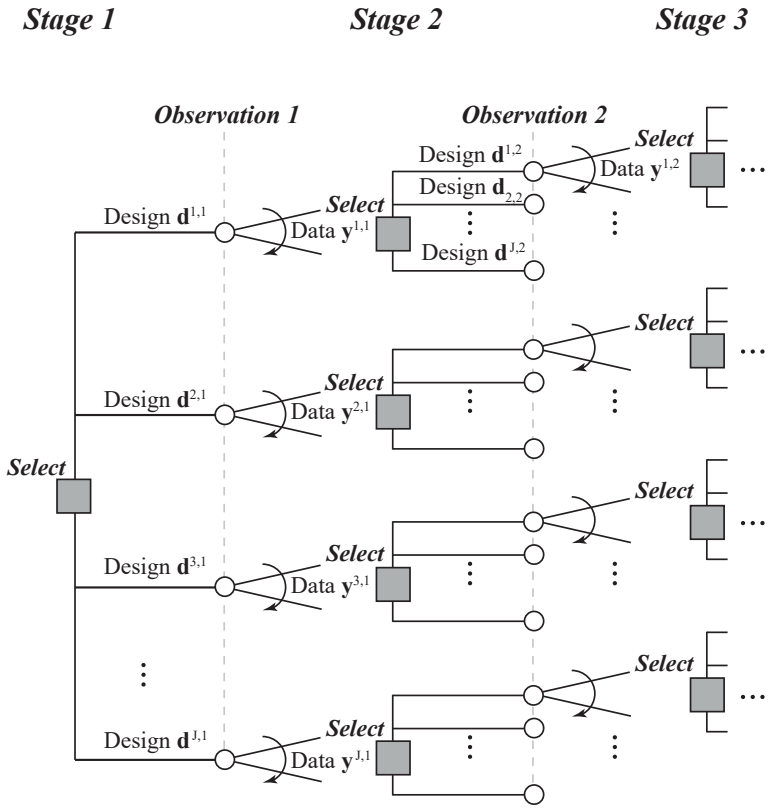


FIG 3. *Optimal sequential path selection.*

a series of intermixed maximisations over designs and integrals over data. In practice, the optimal solution is intractable because of the enormous growth over stages (see e.g. Sucar, Morales and Jesse (2015) and Powell (2016)). Instead, we outline heuristic strategies. In terms of notation, let $\mathcal{Y}^{s-1} = \{d^{j,r}, \boldsymbol{y}^{j,r}; r = 1, \ldots, s-1\}$ denote the data gathered until stage $s-1$, using a selected design $d^{j,r}$, $r = 1, \ldots, s-1$.

6.2. *A Naive Sampling Strategy.* The simplest heuristic for adaptive sampling is to choose the next sampling location based on current EPs. The largest variance in sampling locations indicates higher levels of uncertainty; therefore one selects the design location with an EP closest to 0.5.

At stage $s$, based on the currently available data $\mathcal{Y}^{s-1}$, we fit an updated Gaussian model from Eq. (11) with mean $\boldsymbol{m}^{s-1} = E(\boldsymbol{\xi}|\mathcal{Y}^{s-1})$ and covariance matrix $\boldsymbol{A}^{s-1} = \mathrm{Var}(\boldsymbol{\xi}|\mathcal{Y}^{s-1})$. The next stage of measurements $\boldsymbol{y}^{j,s}$ can be gathered with design $d^{j,s}$, $j = 1, \ldots, J$. The *naive* strategy then selects the design according to:

$$
\begin{aligned}
d^{*,s} &= \mathrm{argmin}_{j\in\{1,\ldots,J\}} |p(\boldsymbol{x}_{d^{j,s}}; \mathcal{Y}^{s-1}) - 0.5|, \\
p(\boldsymbol{x}; \mathcal{Y}^{s-1}) &= P(\xi_T(\boldsymbol{x}) \leq t_T, \xi_S(\boldsymbol{x}) \leq t_S | \mathcal{Y}^{s-1}).
\end{aligned} \tag{26}
$$

This strategy does not account for the uncertainty in the temperature or salinity variables, but is instead applicable only if one design (node) has EPs closer to 0.5 (see Table 1, line two). Additionally, this strategy does not account for spatial correlation. This strategy lacks memory of where it has been and where the uncertainty has been reduced, and is therefore susceptible to local minima.

6.3. *Myopic Path Planning.* The myopic (greedy) strategy which we present here is optimal if we imagine taking only one more stage of measurements. In this selection strategy, there is no anticipation of what the subsequent designs might offer beyond the first stage.

Based on the currently available data $\mathcal{Y}^{s-1}$, we fit an updated GP model. The next stage of measurements $\boldsymbol{y}^{j,s}$, can be gathered with design $d^{j,s}$, $j = 1, \ldots, J$. The selected design is then:

$$
\begin{aligned}
d^{*,s} &= \mathrm{argmin}_{j\in\{1,\ldots,J\}} \left\{ V_{m,\mathrm{upd,j}} \right\}, \\
V_{m,\mathrm{upd}} &\approx \sum_{\boldsymbol{x}\in\mathcal{M}_g} E_{\boldsymbol{y}^{j,s}|\mathcal{Y}^{s-1}} \left( p(\boldsymbol{x}; \mathcal{Y}^{j,s}) \left( 1 - p(\boldsymbol{x}; \mathcal{Y}^{j,s}) \right) \right) \Delta, \\
p(\boldsymbol{x}; \mathcal{Y}^{j,s}) &= P(\xi_T(\boldsymbol{x}) \leq t_T, \xi_S(\boldsymbol{x}) \leq t_S | \boldsymbol{y}^{j,s}, \mathcal{Y}^{s-1}).
\end{aligned} \tag{27}
$$

Note that this strategy gives a sequential conditional version of the formula in Eq. (5). Now $\mathcal{Y}^{s-1}$ is available, and the expectation is with respect

to the conditional density $\pi(\boldsymbol{y}^{j,s}|\mathcal{Y}^{s-1})$. A similar closed-form calculation for expected IBV is hence applicable in Eq. (27) using the updated GP model from stage $s-1$. Once the data is collected for the best design, the GP model is updated again. The mean $\boldsymbol{m}^s$ and covariance matrix $\boldsymbol{A}^s$ are used to compute the next design at stage $s+1$, and so on.

Even though this myopic strategy is non-anticipative, it still gives a reasonable approach for creating designs in many applications. Moreover, it is easily implemented onboard an AUV, using an efficient approach for data updating the GP model and the calculation of the closed-form expected IBV expressions for each subsequent trajectory.

6.4. *Look-ahead Trajectory Planning.* We now extend the myopic strategy to a look-ahead strategy, which is optimal when one can gather only two more stages of measurements. In addition to the next stage of measurements $\boldsymbol{y}^{j,s}$, this look-ahead strategy, anticipates the subsequent design $j_2$ with data $\boldsymbol{y}^{j_2,s+1}$ when choosing the current design $d^{j,s}$. The selected design is:

$$
\begin{aligned}
(28) \qquad d^{*,s} &= \operatorname{argmin}_{j\in\{1,\dots,J\}} \left\{U_{la,\mathrm{upd,j}}\right\}, \\
U_{la,\mathrm{upd},j} &= E_{\boldsymbol{y}^{j,s}|\mathcal{Y}^{s-1}} \left\{\operatorname{argmin}_{j_2\in\{1,\dots,J_2\}} \left[V_{la,\mathrm{upd},j_2}\right]\right\}, \\
V_{la,\mathrm{upd},j_2} &\approx \sum_{\boldsymbol{x}\in\mathcal{M}_g} E_{\boldsymbol{y}^{j_2,s+1}|\mathcal{Y}^{j,s}} \left\{p(\boldsymbol{x};\mathcal{Y}^{j,s+1})\left(1-p(\boldsymbol{x};\mathcal{Y}^{j,s+1})\right)\right\}\Delta, \\
p(\boldsymbol{x};\mathcal{Y}^{j,s+1}) &= P(\xi_T(\boldsymbol{x})\le t_T, \xi_S(\boldsymbol{x})\le t_S|\boldsymbol{y}^{j_2,s+1},\mathcal{Y}^{j,s}).
\end{aligned}
$$

Here, $\mathcal{Y}^{j,s}=\{\boldsymbol{y}^{j,s},\mathcal{Y}^{s-1}\}$ and $\mathcal{Y}^{j,s+1}=\{\boldsymbol{y}^{j_2,s+1},\mathcal{Y}^{j,s}\}$ represent the sets of data variables, and the expectations are calculated with respect to the conditional densities $\pi(\boldsymbol{y}^{j,s}|\mathcal{Y}^{s-1})$ and $\pi(\boldsymbol{y}^{j_2,s+1}|\boldsymbol{y}^{j,s},\mathcal{Y}^{s-1})$.

We solve the first expectation by Monte Carlo sampling of data $\boldsymbol{y}^{j,s}$ from its conditional distribution. For each of these data samples, the second expectation is solved using the closed-form expressions for expected IBV from Section 5.

Even though the strategy looks at two sampling stages, it is only used to find the current best design. When data are collected, the GP model is updated, and the mean $\boldsymbol{m}^s$ and covariance matrix $\boldsymbol{A}^s$ are used to compute the next design at stage $s+1$, now anticipating what stage $s+2$ could offer, and so on.

This look-ahead approach is much more computationally demanding than the myopic strategy, so for practical implementation, we prune paths in the evaluation of Eq. (28). This means that we do not compute all possible branches of the first two stages, as they are indicated in Fig. 3. Instead, we use the myopic strategy to rank the three best designs following the

first stage alone, and for each of these preferred designs, we undertake the look-ahead calculations.

**7. Simulation study.** We now study the properties of the different static and sequential survey designs in a realistic simulated case that emulates the spatial properties of a river plume interacting with coastal water.

7.1. *Modeling.* We use a bivariate GP model for temperature and salinity, where we specify the mean:

$$\boldsymbol{\mu}(\boldsymbol{x}) = E\begin{bmatrix}\xi_T(\boldsymbol{x})\\ \xi_S(\boldsymbol{x})\end{bmatrix} = \begin{bmatrix}\mu_T(\boldsymbol{x})\\ \mu_S(\boldsymbol{x})\end{bmatrix} = \begin{bmatrix}\beta_{T,0} + \beta_{T,1}x_{\text{West}}\\ \beta_{S,0} + \beta_{S,1}x_{\text{West}}\end{bmatrix}. \tag{29}$$

This situation mimics that of a river mouth opening from the south, with the water masses pulled to the east. The regression parameters are $\beta_{T,1} = 0.065$ and $\beta_{S,1} = 0.1$ for the slopes with west coordinate, and $\beta_{T,0} = 5.8$ and $\beta_{S,0} = 29.0$ for the intercept at a chosen reference map coordinate.

The covariance is assumed to be stationary and separable for the two variables. The $2 \times 2$ pointwise covariance matrix is set to:

$$\boldsymbol{\Sigma}(\boldsymbol{x}) = \text{Var}\begin{bmatrix}\xi_T(\boldsymbol{x})\\ \xi_S(\boldsymbol{x})\end{bmatrix} = \begin{bmatrix}0.25^2 & 0.6 \cdot 0.25^2\\ 0.6 \cdot 0.25^2 & 0.25^2\end{bmatrix}. \tag{30}$$

The spatial correlation is of a Matern type {KR: cite or define}:

$$\text{Corr}\left(\begin{bmatrix}\xi_T(\boldsymbol{x})\\ \xi_S(\boldsymbol{x})\end{bmatrix}, \begin{bmatrix}\xi_T(\boldsymbol{x}')\\ \xi_S(\boldsymbol{x}')\end{bmatrix}\right) = \begin{bmatrix}1 & 0.6\\ 0.6 & 1\end{bmatrix}(1+\phi h)\exp(-\phi h), \tag{31}$$

where $h = \sqrt{||\boldsymbol{x} - \boldsymbol{x}'||^2}$ and $\phi = 0.3$ indicates an effective correlation range of about 1200 m. One realization of the random fields representing salinity and temperature is shown in Fig. 4(a) and 4(b). The true ES is a realization from this model as shown in Fig. 4(c).

7.2. *Static and Sequential Sampling Designs.* We compare three different static designs denoted *static_north*, *static_east*, and *static_zigzag* with the three described sequential approaches *naive*, *myopic*, and *look-ahead*. The static sampling paths are pre-determined and cannot be altered and represent the pre-planned strategies used in most current AUV operational survey designs.

For a fixed survey length, a closed form expression for the expected IBV is available as in Eq. (5). However, for the sequential approaches this is not the case. For comparison the properties are therefore evaluated using

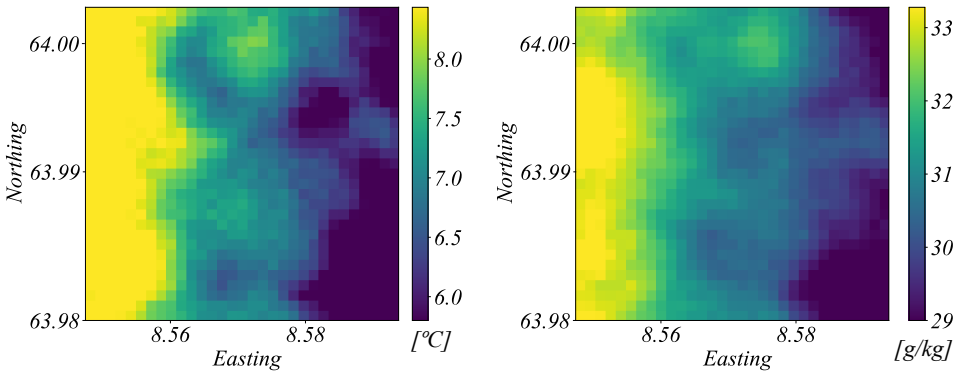


(a) Simulated temperature.

(b) Simulated salinity.

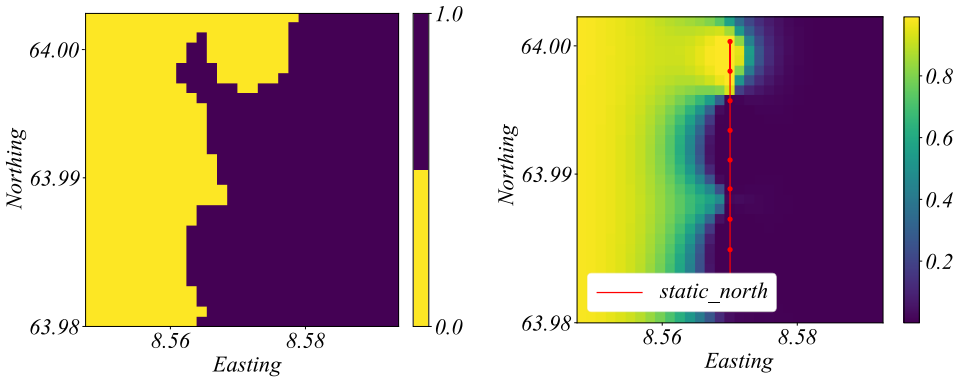


(c) Excursion set given the realization of temperature and salinity.

(d) Excursion probabilities given collected data using the 'static_north" strategy.

FIG 4. *4(a) and 4(b) show a realisation of the simulated temperature and salinity fields. The associated ES is in 4(c), while 4(d) shows the estimated EPs after performing data collection along the static N-S survey line.*

Monte Carlo sampling over several replicates of realizations from the model while conducting simulated sequential surveys for each one. Fig. 4(d) shows the conditional EP, given data gathered along the north-south survey lines in these figures. In the Monte Carlo replicates, such results are repeatedly computed to approximate the expected IBV. We also compare predictive performance measured by root mean square error (RMSE) for temperature and salinity estimates as also the variance reduction in these two variables. It is important to note that the objective function used by the agent is focused on reducing the expected IBV, but we nevertheless expect that we will achieve good predictive performance for criteria such as RMSE as well.

Another non-statistical criteria that is important for practical purposes is the computational time needed for the strategy, as this will impact the performance for an embedded system.

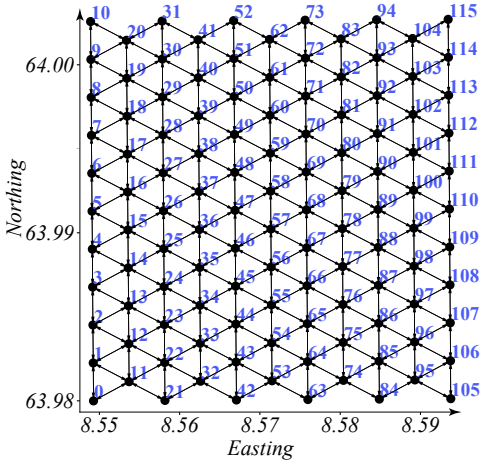


FIG 5. *The equilateral waypoint graph used to discretize the trajectory choices over the* $31 \times 31$ *grid used to discretize the GP.*

Each strategy is conducted on an equilateral grid as shown in Fig. 5. The sequential sampling agent starts at the center East-West coordinate at the southern end of the domain (node 53). The AUV moves along edges in the waypoint graph while the vehicle gathers measurements. The data is assimilated into the GP model before an evaluation of the next node to sample is conducted at the end of the edge.

7.3. *Simulation Results.* A total of 100 replicate simulations were conducted with all strategies. The results are shown in Fig. 6, where the different criteria are plotted as a function of survey distance. Fig. 6(a) shows the resulting drop in IBV for each of the six strategies. IBV reduction occurs most under the *myopic* and *look-ahead* strategies, each performing almost equally; this is expected as the two criteria (Eq. (27) and (28)) are sensitive to differences in IBV. The *static_north* design also does well here because the path is parallel to the boundary between the water masses.

Fig. 6(b) and 6(c) show the resulting drop in RMSE and increase in explained variance, respectively. Both *myopic* and *look-ahead* strategies perform well here, but some of the *static_east* and *static_zigzag* also achieve good results because they are pre-determined to cover large parts of the domain without re-visitation. Sequential strategies targeting IBV will sometimes not reach similar coverage, as interesting data may draw the path into

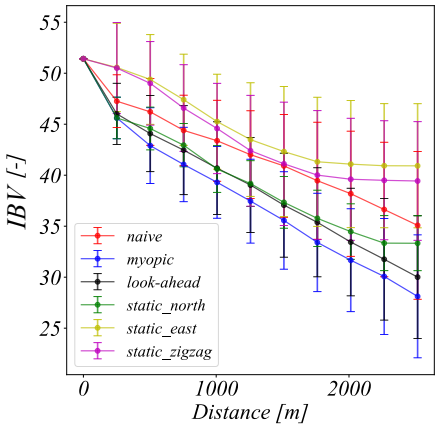


(a) IBV.

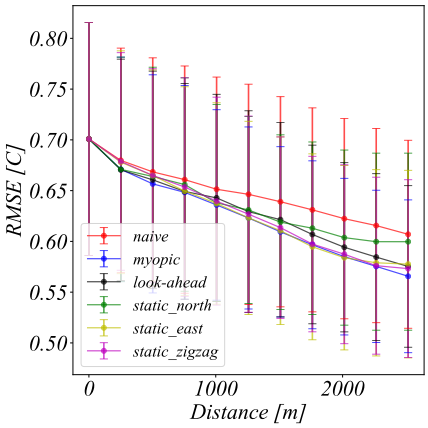


(b) RMSE between estimated field and truth.

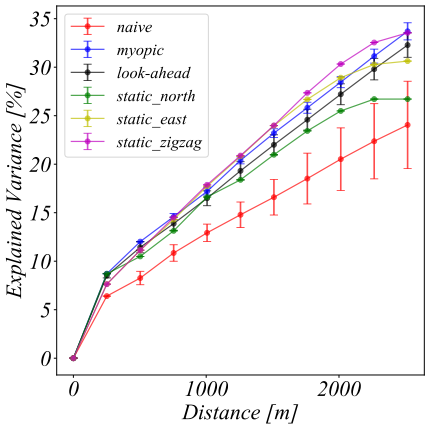


(c) Explained variance $\boldsymbol{R}^2$.

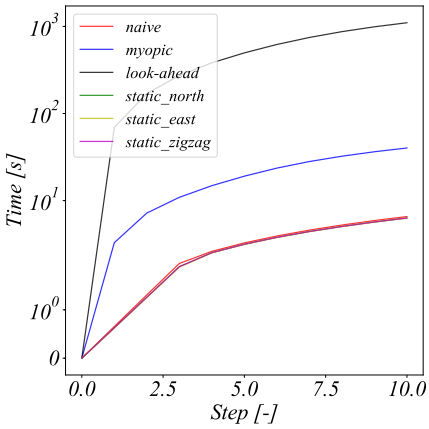


(d) Time used to do inference.

FIG 6. *Simulation results from 100 replicate simulations for 10 sampling choices/stages on the grid.*

twists and turns. There is relatively large variety in the replicate results as indicated by the vertical lines. Nevertheless, the ordering of strategies is similar.

Fig. 6(d) shows the computational effort: the *naive* strategy is on par with the static designs, while the *myopic* strategy is slower. The *look-ahead* is even slower, reaching levels that are nearly impractical for execution on a vehicle.

Some pruning of the graph is performed to improve the computational speed, such as ruling out repeated visitations and back-and-forth routes. Some of the intermediate results are also stored for longer planning horizons. Further pruning of branches or inclusion of other heuristics could be included to make the strategy faster. Then again, the inclusion of heuristics is likely a contributing factor for the *look-ahead* strategy failing to outperform the *myopic* strategy.

In Fig. 7, the realized sampling paths for each of the sequential schemes

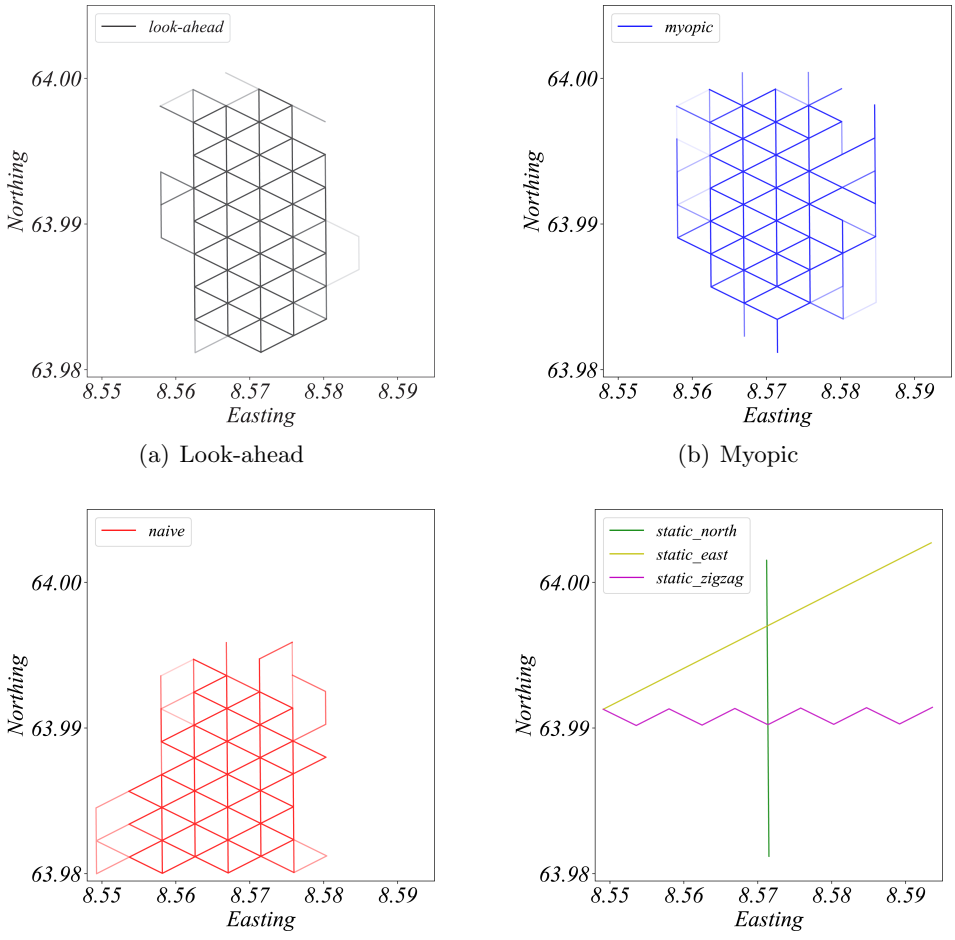


(a) Look-ahead (b) Myopic

(c) Naive (d) Static

FIG 7. *The overlaid route choices (strategies), superimposed on the 100 replicate surveys with 10 sampling choices/stages.*

and static designs are shown. The *naive* strategy often gets stuck in the southern part of the domain because it is too focused on the probabilities near 0.5. The *myopic* strategy covers a wider domain than the naive or look-ahead. There are several reasons for this. First, a greedy approach will tend to put more emphasis on promising locations close to the agent, which may lead away from the centre. Second, as the agent evaluates the impact of locations further away (look-ahead) where assimilated data has less predictive power, the GP model (which is centered here) will act to restrict paths deviating from the central zone.

We studied the sensitivity of the results by modifying the input parameters to have different correlations between temperature and salinity, standard deviations, and spatial correlation range. In all runs, the *myopic* and *look-ahead* strategies perform the best in terms of IBV, and much better than *naive*. The *look-ahead* strategy seems to be substantially better than the *myopic* only for very small initial standard deviation or very large spatial correlation range. The *static_north* design continues to be the best static design for IBV, while *static_zigzag* is the best design for the other predictive performance measures, especially so with large spatial correlation range. We also ran simulation studies with only temperature data, and for realistic correlation levels between temperature and salinity the IBV results are not much worse when only temperature data are available. In addition to the comparison made in Table 1, the current setting includes spatial correlation and this likely reduces the additional influence of having bivariate data. However, it seems that having temperature data alone does a substantially worse job in terms of explained variance

**8. Case Study - Mapping a River Plume.** To demonstrate the applicability of using multivariate EPs and the IBV to inform oceanographic sampling, we present a case study mapping a river plume with an AUV. The experiment was performed in Trondheim, Norway, surveying the Nidelva river (Fig. 1(b)). The experiments were conducted in late Spring 2019, when there is still snow melting in the surrounding mountains so that the river water is substantially colder than the water in the fjord. The experiment was focused along the frontal zone that runs more or less parallel to the eastern shore as noted in Fig. 1(b).

8.1. *Model Specification.* The statistical model parameters were specified based on a short preliminary survey where the AUV made an initial transect to determine the trends in environmental conditions and correlation structures. Based on the initial data, the trend parameters were estimated by linear regression, where both temperature and salinity are assumed to

increase linearly, going west from the river mouth. Next, the residuals from the regression analysis were analyzed to study the fit of the GP model and to specify the covariance parameters.

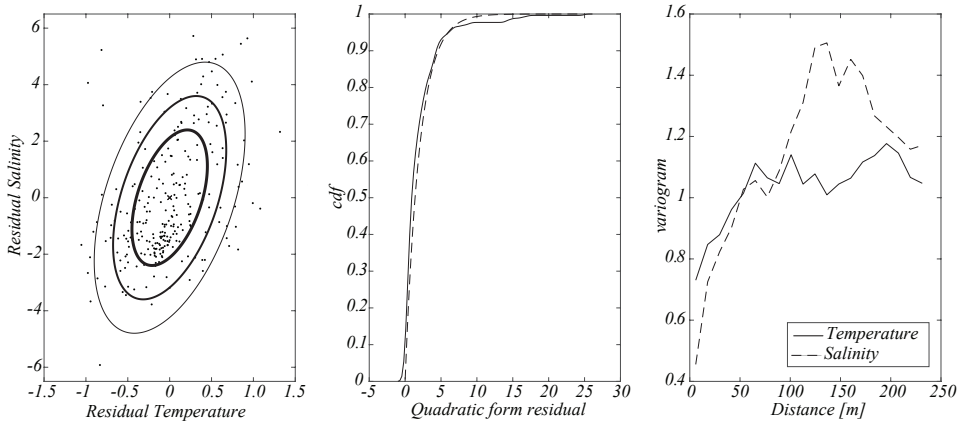


(a) Residual plot. (b) Empirical CDF. (c) Empirical variogram.

FIG 8. *Data analysis from a preliminary trial experiment using the AUV. 8(a) Residual plot of temperature and salinity along with Gaussian contours. 8(b) Empirical CDF (solid) of the quadratic form of the residuals along with the theoretical CDF (dashed) of the* $\chi^2$ *distribution with two degrees of freedom. 8(c) Empirical variogram of the salinity and temperature data.*

Fig. 8 summarizes diagnostic plots of this analysis. Fig. 8(a) shows a cross-plot of temperature and salinity residuals after the westerly trends in both salinity and temperature are subtracted from the data. This scatter-plot of joint residuals indicates larger variability in salinity than in temperature, and a positive correlation (0.5) between the two variables. Based on the fitted bivariate Gaussian model (ellipses in Fig. 8(a)), we can compute the modeled quadratic form of the residuals, and if the model is adequate they should be approximately $\chi^2_2$ distributed. Fig. 8(b) shows the empirical cumulative distribution function (CDF) of these quadratic forms (solid) together with the theoretical CDF of the $\chi^2_2$ distribution. The modeled and theoretical curves are very similar, which indicates that the Gaussian model fits reasonably well. Even though there appears to be some clustering in both Fig. 8(a) and 8(b), the bivariate diagnostic plots look reasonable and justify a Gaussian model. Fig. 8(c) shows the empirical variogram of the scaled residuals for temperature and salinity. The decay is similar for the two, and seems to be negligible after about 150 m.

Based on the analysis in Fig. 8, the resulting parameters are given in Table 2. The regression parameters shown here are scaled to represent the east and

west boundaries of the domain as seen in the preliminary transect data, and the thresholds are intermediate values. These parameter values were then used in field trials where we explored the algorithm's ability to characterize the river plume front separating the river and fjord water masses, providing a spatial map of this boundary.

TABLE 2. *Model and threshold parameters from an initial AUV survey. Observations were taken across the front while crossing from fresh, cold river water to saline and warmer ocean waters.*

| Parameter | Value | Source |
|---|---|---|
| Cross correlation temp. and sal. | 0.5 | AUV observations |
| Temp. variance | 0.20 | AUV observations (variogram) |
| Sal. variance | 5.76 | AUV observations (variogram) |
| Corr. range | 0.15 km | AUV observations (variogram) |
| River temp. $T_{river}$ | 10.0 °C | AUV observations |
| Ocean temp. $T_{ocean}$ | 11.0 °C | AUV observations |
| River sal. $S_{river}$ | 14.0 g/kg | AUV observations |
| Ocean sal. $S_{ocean}$ | 22.0 g/kg | AUV observations |
| Threshold temp. | 10.5 °C | $(T_{ocean} - T_{river})/2 + T_{river}$ |
| Threshold sal. | 18.0 g/kg | $(S_{ocean} - S_{river})/2 + S_{river}$ |

8.2. *Experimental Setup.* The sampling locations were distributed over an equilateral grid, as shown in the grey-colored lattice in Fig. 10(a). The robotic platform consisted of a Light AUV (Sousa et al., 2012) (Fig. 9) equipped with a 16 Hz Seabird Fastcat-49 conductivity, temperature, and depth (CTD) sensor providing temperature and salinity measurements. The sampling agent was built on top of the autonomous agent framework Teleo-Reactive EXecutive (*T-REX*) (Py, Rajan and McGann, 2010; Rajan and Py, 2012; Rajan, Py and Berreiro, 2012), running an instance of the *myopic* strategy from Section 6.3 to control the AUV and decide between sampling locations.


FIG 9. *The commercially available Light Autonomous Underwater Vehicle (LAUV) platform for upper water-column exploration used in our experiments.*

The sampling strategy was designed around the concept of visiting way-

points sequentially. Arriving at a desired waypoint with new measurements and an updated model, the AUV triggers the myopic strategy to evaluate the different design criteria (see Eq. (27)). The waypoint-and-path combination that is expected to reduce the IBV the most is selected, and upon arrival this procedure is then repeated. At each stage, it takes the AUV about 30 seconds to evaluate the expected IBV for all the possible waypoint-and-path alternatives.

The AUV was set to start in the south-center part of the waypoint graph, with the previously outlined GP model of the environment (Section 8.1). A survey was set to take approximately 40 minutes, visiting 15 waypoints on the grid, with the AUV running near the surface to capture the plume. On its path from one waypoint to the next, the AUV gathered data regularly, and the GP model assimilated temperature and salinity data with an update frequency of 30 seconds, giving about three updates per stage.

8.3. *Results.* Two missions, Surveys 1 and 2, were run successively from 11:00 AM to 01:00 PM, with a short break in between. The resulting path of the selected waypoints are shown in the map in Fig. 10(a), both within the expected frontal region (shaded pink). The recorded temperatures are shown as colored trails in Fig. 10(b), clearly indicating the temperature difference between fjord and river waters. The salinity data are then shown separately, overlaid with the estimated EP for each survey in Fig. 10(c) and 10(d).

Both surveys successfully estimated and navigated the separation zone, crossing the frontal boundary multiple times. As conditions changed slightly between the two deployments, the resulting path (after waypoint 5) is shown to deviate. Survey 1 continued northwards, tracking the north-eastern part of the front, while Survey 2 turned west, mapping the south-western part.

The final predictions of the front location, represented by conditional EPs in Fig. 10(c) and 10(d) as dashed lines, correspond with one another. In both surveys they yield a picture of the front being a bit to the west in the southern parts of the domain and gradually bending off toward the north east. The amount of exploration done by Survey 1 is greater than Survey 2. In Survey 1, the AUV obtained more detail by going north from waypoint 5, while Survey 2, coming close to the survey area borders in the south-western corner, obtained a poorer understanding of the northern parts. A look-ahead strategy might identify and discourage such choices.

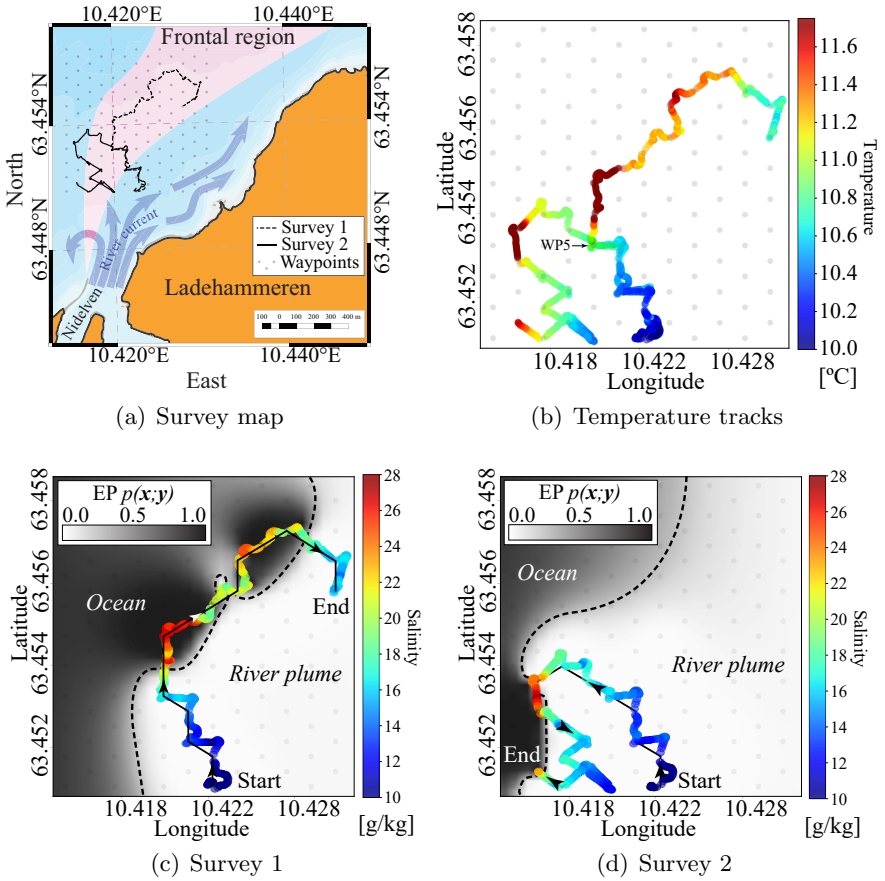


(a) Survey map (b) Temperature tracks

(c) Survey 1 (d) Survey 2

FIG 10. *Results from mapping the Nidelva river. 10(a) Show an overview of the survey area overlaid with the AUV path in black and dashed line. Note the shaded region indicating the usual frontal region. 10(b) Presents the collected temperature data as colored trails. Note waypoint 5 (WP5) which indicate where the two surveys deviate. 10(c) and 10(d) Shows the collected salinity data (as a colored trail) overlaid on the final EP, which indicate the AUVs statistical impression of the front. For both missions the temperature and salinity data correspond with the EP front indication.*

**9. Closing remarks.** This work builds on a multidisciplinary effort combining statistical modeling with robotic surveying techniques for oceanographic applications. We show how observation practices can gain efficiency and accuracy from the development of statistical techniques to achieve more effective spatial monitoring. We further demonstrate the opportunities available for real-time multivariable spatial data-gathering and analysis onboard autonomous sensing platforms, which statisticians can exploit to create general-purpose toolkits for similar applications.

In particular, we derive and show results for characterizing phenomena connected to the properties of water masses. The characterization is based on joint ESs, whereby we derive new results for the expected IBV reduction achieved by the spatial sampling design. This result is first calculated in closed form for the situation with a static design, and then extended to the adaptive situation. The sequential derivations provide new insights into efficient applications of adaptive sampling, as demonstrated in our application of these models with an autonomous vehicle in Trondheim fjord.

The study did not consider any temporal effects, which would be relevant on a larger time scale. We consider the extension to spatio-temporal modeling as future work, and envision that advection-diffusion equations could be useful in this kind of modeling (Sigrist, Künsch and Stahel, 2015). For more complex oceanographic phenomena, the methods will need to be extended to non-Gaussian phenomena, possibly feature-based mixtures of GPs which could still be run onboard and augmented by dynamical models.

The spatial-statistical design criterion, building on ESs, is relevant in our setting with different water mass properties; this could also be useful in other oceanographic settings, such as algal-blooms or open water fronts. Of course, other criteria are also relevant for decision-making. For instance, managers and regulators must make difficult decisions related to fish farming, other marine resources operations, or environmental projects. Value of information analysis (VOI) (Eidsvik, Mukerji and Bhattacharjya, 2015) could be used in a similar vein as the IBV in the current paper, as both analytic methods explore when, where and which information is likely to result in improved decision-making.

While more effort could be spent on approximating the look-ahead stages in the adaptive designs, it is perhaps more interesting to explore the additional flexibility that can be gained by having two or more AUVs cotemporally exploring a spatial or spatio-temporal domain together (Ferreira et al., 2019). Such an approach would enable concurrent sampling in different parts of the space, or opportunities to move in parallel to best capture the excursion set.

**Acknowledgements.** TOF and KR acknowledge support from the Centre for Autonomous Marine Operations and Systems (AMOS)[2], Center of Excellence, project number 223254, and the Applied Underwater Robotics Labortatory (AURLab). JE acknowledges support from Norwegian research council project 294404. DG acknowledges support from the Swiss National Science Foundation, project number 178858.

[2] https://www.ntnu.edu/amos

## References.


Costa, M. J., Pinto, J., Dias, P. S., Pereira, J., Lima, K., Ribeiro, M., Sousa, J. B., Lukaczyk, T., Mendes, R., Tomasino, M. P., Magahlaes, C., Belkin, I., Lopez-Castejon, F., Gilabert, J., Skarpnes, K. A., Ludvigsen, M., Rajan, K., Mirmalek, Z. and Chekalyuk, A. (2018). Field Report: Exploring Fronts with Multiple Robots. In *IEEE AUV*.

Azzimonti, D., Bect, J., Chevalier, C. and Ginsbourger, D. (2016). Quantifying uncertainties on excursion sets under a Gaussian random field prior. *SIAM/ASA Journal on Uncertainty Quantification* **4** 850–874.

Bect, J., Bachoc, F. and Ginsbourger, D. (2019). A supermartingale approach to Gaussian process based sequential design of experiments. *Bernoulli* **25** 2883–2919.

Bect, J., Ginsbourger, D., Li, L., Picheny, V. and Vazquez, E. (2012). Sequential design of computer experiments for the estimation of a probability of failure. *Statistics and Computing* **22** 773–793.

Bellingham, J. G. and Rajan, K. (2007). Robotics in Remote and Hostile Environments. *Science* **318** 1098-1102.

Bhattacharjya, D., Eidsvik, J. and Mukerji, T. (2013). The value of information in portfolio problems with dependent projects. *Decision Analysis* **10** 341–351.

Binney, J., Krause, A. and Sukhatme, G. S. (2013). Optimizing waypoints for monitoring spatiotemporal phenomena. *The International Journal of Robotics Research* **32** 873–888.

Bolin, D. and Lindgren, F. (2015). Excursion and contour uncertainty regions for latent Gaussian models. *Journal of the Royal Statistical Society: Series B (Statistical Methodology)* **77** 85–106.

Chevalier, C., Bect, J., Ginsbourger, D., Vazquez, E., Picheny, V. and Richet, Y. (2014). Fast parallel kriging-based stepwise uncertainty reduction with application to the identification of an excursion set. *Technometrics* **56** 455–465.

Coriolis, G. G. (1835). *Mémoire sur les équations du mouvement relatif des systèmes de corps*. Bachelier.

Das, J., Py, F., Maughan, T., Messie, M., O'Reilly, T., Ryan, J., Sukhatme, G. S. and Rajan, K. (2012). Coordinated Sampling of Dynamic Oceanographic Features with AUVs and Drifters. *International Journal of Robotics Research* **31** 626-646. April.

Das, J., Py, F., Harvey, J. B. J., Ryan, J. P., Gellene, A., Graham, R., Caron, D. A., Rajan, K. and Sukhatme, G. S. (2015). Data-driven robotic sampling for marine ecosystem monitoring. *The International Journal of Robotics Research* **34** 1435–1452.

Eidsvik, J., Mukerji, T. and Bhattacharjya, D. (2015). *Value of Information in the Earth Sciences: Integrating Spatial Modeling and Decision Analysis*. Cambridge University Press, Cambridge.

Ferreira, A. S., Costa, M., Py, F., Pinto, J., Silva, M. A., Nimmo-Smith, A., Johansen, T. A., de Sousa, J. B. and Rajan, K. (2019). Advancing multi-vehicle deployments in oceanographic field experiments. *Autonomous Robots* **43** 1555–1574.

Fossum, T. O., Eidsvik, J., Ellingsen, I., Alver, M. O., Fragoso, G. M., Johnsen, G., Mendes, R., Ludvigsen, M. and Rajan, K. (2018). Information-driven robotic sampling in the coastal ocean. *Journal of Field Robotics* **35** 1101-1121.

Fossum, T. O., Fragoso, G. M., Davies, E. J., Ullgren, J. E., Mendes, R., Johnsen, G., Ellingsen, I., Eidsvik, J., Ludvigsen, M. and Rajan, K. (2019). Toward adaptive robotic sampling of phytoplankton in the coastal ocean. *Science Robotics* **4**.

French, J. P. and Hoeting, J. A. (2016). Credible regions for exceedance sets of geostatistical data. *Environmetrics* **27** 4–14.

French, J. P., Sain, S. R. et al. (2013). Spatio-temporal exceedance locations and confidence regions. *The Annals of Applied Statistics* **7** 1421–1449.

Genton, M. G., Kleiber, W. et al. (2015). Cross-covariance functions for multivariate geostatistics. *Statistical Science* **30** 147–163.

Genz, A. and Bretz, F. (2009). *Computation of multivariate normal and t probabilities* **195**. Springer Science & Business Media.

Gneiting, T., Kleiber, W. and Schlather, M. (2010). Matérn cross-covariance functions for multivariate random fields. *Journal of the American Statistical Association* **105** 1167–1177.

Gottlieb, J., Graham, R., Maughan, T., Py, F., Elkaim, G. and Rajan, K. (2012). An Experimental Momentum-based Front Detection for Autonomous Underwater Vehicles. In *IEEE International Conference on Robotics and Automation (ICRA)*.

Lermusiaux, P. F. J. (2006). Uncertainty Estimation and Prediction for Interdisciplinary Ocean Dynamics. *J. Comput. Phys.* **217** 176–199.

Low, K. H., Dolan, J. M. and Khosla, P. K. (2009). Information-Theoretic Approach to Efficient Adaptive Path Planning for Mobile Robotic Environmental Sensing. *Proceedings of the International Conference on Automated Planning and Scheduling* 233–240.

Mellucci, C., Menon, P. P., Edwards, C. and Challenor, P. (2018). Oceanic Feature Boundary Mapping with an Autonomous Underwater Glider. In *2018 Annual American Control Conference (ACC)* 5338–5343. IEEE.

Munk, W. (2002). The Evolution of Physical Oceanography in the Last Hundred Years. *Oceanography* **15**.

Picheny, V., Ginsbourger, D., Roustant, O., Haftka, R. T. and Kim, N.-H. (2010). Adaptive designs of experiments for accurate approximation of a target region. *Journal of Mechanical Design* **132** 071008.

Pinto, J., Mendes, R., da Silva, J. C. B., Dias, J. M. and de Sousa, J. B. (2018). Multiple Autonomous Vehicles Applied to Plume Detection and Tracking. In *2018 OCEANS - MTS/IEEE Kobe Techno-Oceans (OTO)* 1-6.

Powell, W. B. (2016). Perspectives of approximate dynamic programming. *Annals of Operations Research* **241** 319–356.

Py, F., Rajan, K. and McGann, C. (2010). A Systematic Agent Framework for Situated Autonomous Systems. In *9th International Conf. on Autonomous Agents and Multiagent Systems (AAMAS)*.

Rajan, K. and Py, F. (2012). T-REX: Partitioned Inference for AUV Mission Control. In *Further Advances in Unmanned Marine Vehicles* (G. N. Roberts and R. Sutton, eds.) The Institution of Engineering and Technology (IET).

Rajan, K., Py, F. and Berreiro, J. (2012). Towards Deliberative Control in Marine Robotics. In *Marine Robot Autonomy* (M. Seto, ed.) Springer Verlag.

Sahu, S. K. and Challenor, P. (2008). A space-time model for joint modeling of ocean temperature and salinity levels as measured by Argo floats. *Environmetrics: The official journal of the International Environmetrics Society* **19** 509–528.

Sigrist, F., Künsch, H. R. and Stahel, W. A. (2015). Stochastic partial differential equation based modelling of large space–time data sets. *Journal of the Royal Statistical Society: Series B (Statistical Methodology)* **77** 3–33.

Singh, A., Krause, A., Guestrin, C. and Kaiser, W. J. (2009). Efficient informative sensing using multiple robots. *Journal of Artificial Intelligence Research* **34** 707–755.

Sousa, A., Madureira, L., Coelho, J., Pinto, J., Pereira, J., Sousa, J. and Dias, P.

(2012). LAUV: The man-portable autonomous underwater vehicle. In *Navigation, Guidance and Control of Underwater Vehicles* **3** 268–274.

Stroh, R. (2018). Planification d'expériences numériques en multi-fidélité: Application à un simulateur d'incendies, PhD thesis, Université Paris-Saclay.

Sucar, L. E., Morales, E. F. and Jesse, H. (2015). Probabilistic graphical models. *Advances in Computer Vision and Pattern Recognition. London: Springer London. doi* **10** 978–1.

Wikle, C. K., Milliff, R. F., Herbei, R. and Leeds, W. B. (2013). Modern statistical methods in oceanography: A hierarchical perspective. *Statistical Science* 466–486.

Zhang, Y., Godin, M. A., Bellingham, J. G. and Ryan, J. P. (2012). Using an autonomous underwater vehicle to track a coastal upwelling front. *IEEE Journal of Oceanic Engineering* **37** 338–347.

[redacted]
Trygve Olav Fossum
Department of Marine Technology
Otto Nielsens veg. 10, 7491 Trondheim
Norway
E-mail: trygve.o.fossum@ntnu.no

Jo Eidsvik
Department of Mathematical Sciences
Hogskoleringen 1, 7491 Trondheim
Norway
E-mail: jo.eidsvik@math.ntnu.no

David Ginsbourger
Idiap Research Institute
Rue Marconi 19, 1920 Martigny
Switzerland
E-mail: david.ginsbourger@idiap.ch

Kanna Rajan
Department of Engineering Cybernetics
O. S. Bragstads Plass 2D, 7034 Trondheim
Norway
E-mail: kanna.rajan@ntnu.no